optica

Gas-induced differential refractive index enhanced guidance in hollow-core optical fibers

T. W. Kelly,* P. Horak, I. A. Davidson, M. Partridge, G. T. Jasion, S. Rikimi, A. Taranta, D. J. Richardson, F. Poletti, and N. V. Wheeler

Optoelectronics Research Centre, Zepler Institute of Photonics and Nanoelectronics, University of Southampton, Southampton SO17 1BJ, UK
**Corresponding author: twk1g15@soton.ac.uk*

Received 11 March 2021; revised 7 May 2021; accepted 13 May 2021 (Doc. ID 424224); published 16 June 2021

Hollow-core fibers (HCFs) are a potentially transformative fiber technology, where light is confined within a hollow core surrounded by a cladding composed of air holes defined by glass membranes. Dramatic reductions in the minimum losses achieved in a HCF are driving forward their application in low-latency data transmission and ultra-high-power delivery, and maximizing their performance is of increasing interest. Here, we demonstrate that introducing an extremely small gas-induced differential refractive index (GDRI) between the gas within the core and cladding regions of a HCF enables dramatic changes to a HCF's optical properties, including loss, bend loss, and modality. Within this work, we focus on a tubular HCF and demonstrate through experiment and simulations that the confinement loss of this fiber can be reduced by a factor of 5 using a differential pressure of only 6.7 bar. Understanding GDRI is critical for applications where the gas content within the fiber is actively controlled. Moreover, GDRI provides a new means to control the optical properties of a HCF post-fabrication, opening up new areas of design space and providing a tool to tailor and enhance the optical performance of even state-of-the-art HCFs.

https://doi.org/10.1364/OPTICA.424224

1. INTRODUCTION

Hollow-core guidance reduces nonlinearity, increases bandwidth, and offers a route to ultra-low loss in optical fibers [1–3]. HCFs also provide an enhanced path length for gas–light interactions, as the core-guided light interacts with the gas over the entire fiber length. This feature has been extensively exploited for gas detection [4–6], non-linear optics [7,8], and light generation [9,10]. Furthermore, actively controlling the gas content within the core and cladding holes provides a means to tailor the fiber's dispersion post-fabrication [10].

To optimize a HCF's attenuation, bend loss, and modality [11–13], several structural parameters, including the cladding tube number and size, can be modified during the fiber's design and fabrication. However, these geometry modifications are limited by performance trade-offs in fiber design and fabrication constraints [14,15], and an alternative approach for modifying a HCF's optical properties is of great interest.

Here, for the first time to our knowledge, we explore a new regime whereby the gas content within the core of a HCF is controlled independently from that in the cladding holes to create a gas-induced differential refractive index (GDRI) between the core and cladding holes. This can be achieved experimentally by filling these regions with gases of differing pressures and/or compositions. We show through both experiment and simulation that GDRI significantly modifies a HCF's fundamental optical properties, including attenuation, modality, and bend loss.

2. PRINCIPLE OF OPERATION

To elucidate the impact of GDRI on the optical properties of a HCF, we first consider a simplified model of optical guidance. Figure 1(a) shows a scanning electron microscope (SEM) image of a tubular hollow core antiresonant fiber (HC-ARF) which is used throughout this paper. For key structural parameters for this fiber, along with simulated and experimental loss measurements, see Fig. S1 of Supplement 1 The core typically supports many air-guided modes, as do the smaller cladding tubes, but due to the close proximity of the cladding to the fiber jacket inner boundary, cladding modes are highly lossy. If the effective indices of a core and cladding mode are similar, phase-matching leads to an increase in the loss of the core mode as it resonantly couples to the higher-loss cladding mode. Therefore, to achieve low loss, the core must support modes with a higher effective index than the cladding.

If we approximate the fiber core as a circular capillary, the modal effective index, as a function of the gas refractive index n_{gas} at pressure P, temperature T, wavelength λ, and capillary radius r, can be calculated analytically by [16]:

$$n_{nm} = \sqrt{n_{\mathrm{gas}}^2(\lambda,\, P,\, T) - \frac{u_{nm}^2}{4\pi^2}\left(\frac{\lambda}{r}\right)^2}, \tag{1}$$

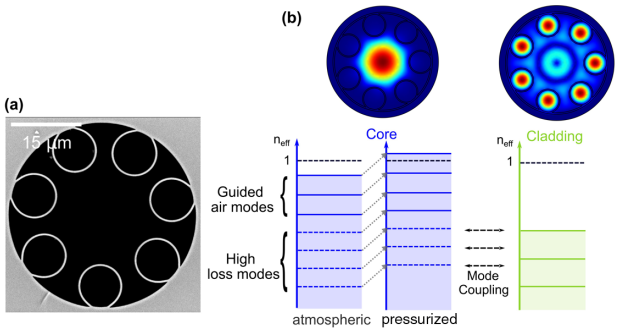

Fig. 1. (a) Scanning electron micrograph (SEM) image of the tubular fiber used in this work. (b) (top) Simulated mode field profiles of the fundamental core and cladding modes of the HC-ARF in (a); (bottom) Schematic representation of relative effective indices for the core and cladding modes in a HC-ARF, with the core at atmospheric and elevated pressure. The raised core pressure induces an increase in the core refractive index, which alters the core-to-cladding mode coupling, impacting the fiber's optical properties.

where u_{nm} is the mth zero of the nth-order Bessel function of the first kind. The conventional approach to control coupling between the core and cladding modes of a HCF focuses on geometry; for example, the core will support modes with effective indices higher than the cladding if its diameter is larger than that of the cladding holes. However, changing n_{gas} via gas pressure or composition offers another approach.

To illustrate the concept, in the following, we consider the case of a tubular fiber with seven tubes, like the fabricated fiber shown in Fig. 1(a). Using Eq. (1), the difference between the effective indices (Δn_{01}) for an LP_{01} mode guided in a capillary of radius 10.25 and 4.35 μm (corresponding to core and cladding tubes, respectively) is $\Delta n_{01} = 0.0054$ (for 1.3 μm wavelength and Argon at s.t.p.). Increasing the core pressure to 10 bar (increasing n_{gas}) raises the modal effective index by 0.0023, and Δn_{01} increases to 0.0077. While small, this change is sufficient to dramatically alter mode coupling and therefore the optical properties of the HCF; this is shown schematically in Fig. 1(b).

3. NUMERICAL AND EXPERIMENTAL RESULTS

We first quantify the impact of GDRI on the optical properties of the fiber in Fig. 1(a) by numerical simulations. The modes of this fiber were solved using a fully vectorial finite element solver (COMSOL Multiphysics). To implement GDRI, the fiber's core and cladding are pressurized with Argon gas to define a differential pressure, both negative (positive), where the cladding (core) pressure is raised and the core (cladding) kept at one bar.

The contour plots in Figs. 2(a) and 2(b) show the variation in confinement loss (CL) in the first (near-IR) and second (visible) transmission windows as a function of wavelength and differential pressure (note logarithmic scale). The top panels show the calculated change in CL with differential pressure, normalized to the loss with zero applied differential pressure for a few selected wavelengths. Notably, *GDRI enables a* $>$ *5x loss* reduction towards the short wavelength edge of the first window and across the second transmission window. While only CL is considered here, this tends to be the dominant loss mechanism in state-of-the-art HC-ARFs.

Figure 3(a) shows higher-order mode (HOM) loss as a function of differential pressure at 1.3 μm; pressurizing the core (positive differential pressure) reduces the loss of all core-guided

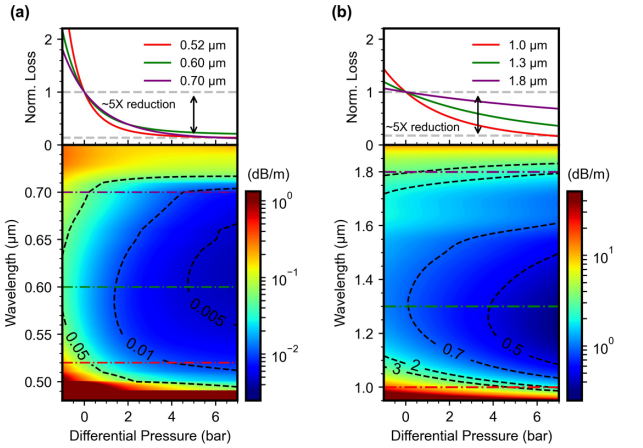

Fig. 2. (a) Simulation results for tubular HCF considering elevated core and cladding pressures. Contour plot of simulated confinement loss (fundamental mode) across the visible guidance window with wavelength and differential pressure. Top panel: loss plotted for various wavelengths (indicated by corresponding dashed lines on the contour plot) with differential pressure, normalized to the loss when both the core and cladding are at equal (atmospheric) pressure. (b) As (a) but for the near-IR transmission window.

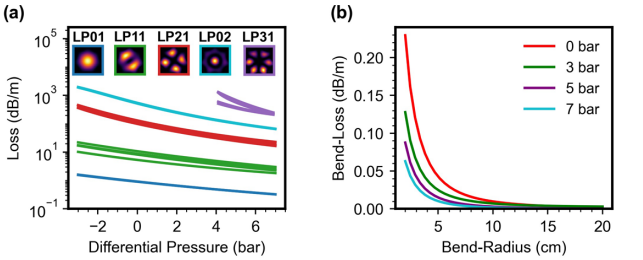

Fig. 3. (a) Modal confinement loss with differential pressure at 1.3 μm. (b) Simulated bend loss for selected values of differential core pressure at 1.3 μm.

modes. Similarly, Fig. 3(b) indicates significant reduction in bend sensitivity as the core pressure is elevated; bend loss is a performance-limiting factor for tubular HCFs in applications which require coiled fiber, such as gyroscopes or compact gas sensors.

To verify these simulations, the near-IR transmission of 25 m of the tubular HCF shown in Fig. 1(a) was measured while being filled with Argon gas from one end (at a gauge pressure of 6.7 bar via a gas cell equipped with an optical window; see Fig. S2 of Supplement 1) while the other end was at atmospheric pressure.

For this initial experiment, the cladding holes were sealed so the gas solely pressurized the core. The measured near-IR transmission at atmospheric and raised average core pressure [see Methods, Eq. (5)] is shown in Fig. 4(a), clearly demonstrating a substantial increase in the transmitted power and spectral bandwidth for the latter case. The change in measured power between atmospheric and raised average core pressure is also plotted here and indicates an improvement of ∼10 dB at a wavelength of 1.3 μm. The change in transmission predicted by the numerical modeling is also shown and is in excellent agreement for simulation parameters closely matching the experimental conditions (see Methods).

Figure 4(b) shows the change in fiber attenuation with time for three wavelengths within the first transmission window. As the core is pressurized, the transmitted power rapidly increases, reaching

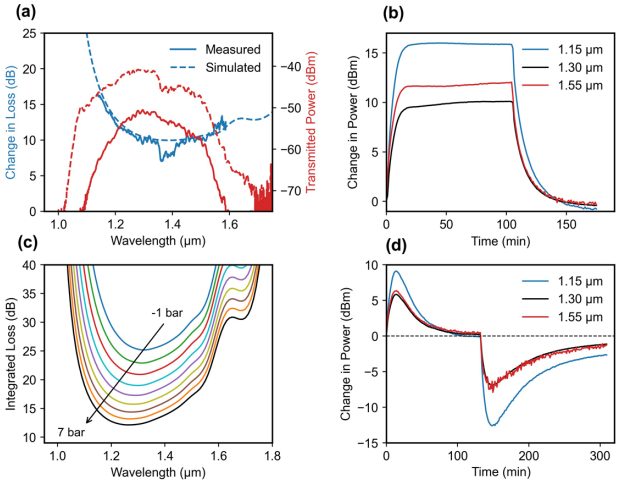

Fig. 4. (a) Measured near-IR transmission window (solid red curve) for zero differential pressure (core and cladding atmospheric pressure), and for a gauge pressure of 6.7 bar at one end of 25 m of tubular HC-ARF, and atmospheric pressure at the other end (dashed red curve). The solid blue curve shows the change in transmitted power calculated from these experimental results and the dashed blue curve shows the simulated change in loss considering the experimental conditions. The feature between ∼1.35 and 1.40 μm is due to absorption by residual water vapor within the introduced Argon gas. (b) Measured change in transmitted power versus time for three selected wavelengths, while the fiber core is pressurized [from 0 minutes and using the same experimental setup as in (a)] and then while both ends are vented to atmosphere (from 106 min). Note that at 1.15 μm, the curve dips below zero; this is attributed to greater instability of the supercontinuum source at this wavelength. (c) Simulated loss integrated over a 25 m length (considering pressure gradient along core, see Methods, to reflect the experiment) against wavelength for various inlet pressures (1 bar steps). (d) Transmitted power over three wavelengths during pressurization and subsequent venting of both core and cladding using the same fiber and experimental conditions as (a) (but without the cladding holes being sealed). Note that the filling process started at 0 min and, after the fiber transmission had stabilized, the venting process started at ∼130 min. Note also the contrast to the behavior depicted in (b).

∼90% of its maximum value after ∼10 min, then plateauing once the core fills completely. The fiber permanently remains in this "low loss" state due to the increased confinement of the guided mode. After ∼105 min, the core is vented and the transmitted power falls back to its initial state, demonstrating the complete reversibility of this process (for animation, see Visualization 1.

Figure 4(c) shows the simulated loss integrated over a 25 m fiber length for several core pressures and highlights that even a small differential pressure (<1 bar) is enough to see a measurable change in the attenuation and bandwidth.

Next, we performed a second experiment in which the cladding holes were also open to a change in pressure. The change in transmission with time as gas pressure was applied to both the core and cladding holes is shown in Fig. 4(d). At the beginning of the filling process, the transmitted power rose; it then peaked and after some time started decaying back to its initial state, which it reached after ∼130 min. At 130 min, the HCF was vented (to atmosphere) and the reverse happened but over a longer time scale. This behavior, which sharply contrasts the sealed cladding hole case, can be attributed to the interplay between the filling dynamics of the core and cladding. Specifically, as the core diameter is ∼2 times that of the average cladding capillary, it initially fills ∼4 times faster [17]; during this time, the core has a higher refractive index than the cladding and hence confinement loss is reduced. The average pressure in the capillary tubes will then continue to rise, even after the core pressure reaches steady state, until it equalizes, eliminating the refractive index difference and returning the fiber attenuation to its original value. Conversely, when the fiber vents to atmosphere, the core empties at a faster rate such that its pressure (and hence refractive index) are lower, increasing the fiber attenuation until a steady state is reached. These transient changes in the optical properties of a HCF, as both the fiber core and cladding regions fill, are extremely important for any application which requires the HCF to be filled with gas—for example, for high sensitivity gas detection [5]. Until now, the filling time for a HCF typically only considered the time to fill the fiber core; here, we show that the filling time of the cladding holes (which is usually notably longer) should also be considered.

4. IMPACT OF CAPILLARY SIZE

Here, we begin to extend this study. To compare the impact of GDRI and cladding capillary size for the fiber design discussed so far, a range of geometries with varying capillary sizes was modeled (Fig. 5). The core radius R, the number of tubes and their thickness, t, were kept constant at 10.25 μm and 446 nm respectively, while the capillary tube inner radius r was varied from small capillaries 0.292 times the core size up to the largest possible capillaries the structure can house without them contacting.

Figure 5(a) shows the variation in CL with differential pressure and r/R (see Fig. S4 of Supplement 1 for CL in the visible at 620 nm). For differential pressures in the range from −1 to 1 bar, the CL reaches a minimum for $r/R \sim 0.55$ and then begins to increase for higher r/R (corresponding to larger capillaries), due to increasing coupling between core and cladding modes. For an applied differential pressure greater than ∼1 bar, the relative increase in the effective indices of the core modes compared to

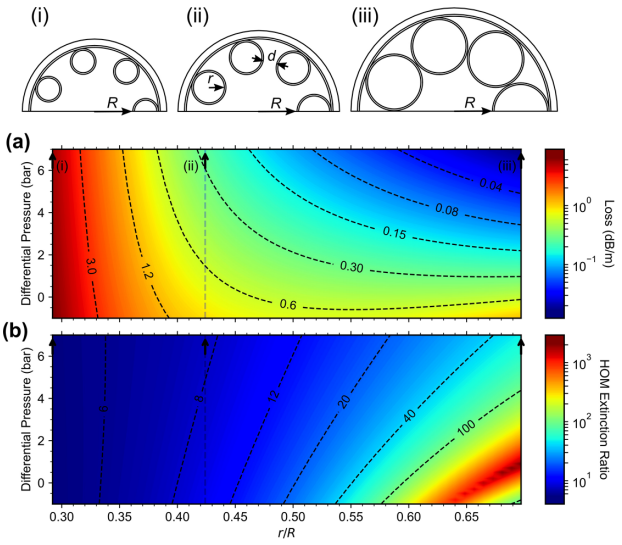

Fig. 5. (a) Effect of both pressurization and cladding tube size on the loss of the fundamental mode, and (b) HOM extinction ratio (ratio of losses between the lowest-loss LP_{11} HOM and the fundamental mode) for an idealized tubular HC-ARF. The x axis is capillary inner radius, r, normalized to the core radius R. The core radius, membrane thickness t, and wavelength were all kept fixed at 10.25 μm, 446 nm, and 1.3 μm, respectively. The top panel shows structures corresponding to r/R values of 0.292, 0.424, and 0.697, and their respective positions are indicated on the contour plot.

the cladding modes reduces core–cladding mode coupling such that CL significantly reduces and the minimum CL value shifts to higher r/R.

The tubular HC-ARF in Fig. 1(a) has a similar design to that in Fig. 5(ii), where the ratio between the loss at 7 and 0 bar of differential pressure is 2.8. With a very large r/R ratio of 0.697, Fig. 5(iii), an even greater reduction in loss is predicted, with a ratio as high as ∼33. While these ratios and the required pressure are specific to this fiber structure, these simulations give an idea of the impact of GDRI as a function of different fiber design parameters.

Figure 5(b) shows the HOM extinction ratio, defined as the ratio of losses between the lowest-loss LP_{11} HOM and the fundamental mode. For high r/R values, this ratio decreases substantially with increasing core pressure, again highlighting that HOMs can be supported with lower loss and that for designs with large capillaries, Fig. 5(iii), the HOM extinction ratio can be decreased by $>10\times$ using GDRI. It is desirable to decrease the HOM extinction ratio for several applications including, for example, where these fibers are used for mode division multiplexing, utilizing the fiber modes as separate communication channels [18].

This demonstrates a key aspect of GDRI: while it is possible to reduce the capillary size to create the same Δn_{01} as achieved by raising the core pressure, the loss via this conventional approach is much greater due to the closer proximity of the core to the glass jacket. GDRI therefore allows multi-mode HCFs to have more low-loss HOMs.

Within this paper, we have focused on tubular anti-resonant HCFs. However, it should be noted that GDRI will also impact the optical properties of other HCF designs, including the latest Nested Antiresonant Nodeless Fibers (NANFs), which are now moving very close to achieving similar losses to conventional silica fibers [1]. Studying the impact of GDRI in other HCF designs and investigating the potential of GDRI as a tool to further enhance the optical properties of these HCFs will be further investigated in future work.

5. CONCLUSIONS AND OUTLOOK

In conclusion, we have demonstrated that a very small refractive index change induced by different refractive indices between the gases in the core and cladding regions of a HC-ARF can significantly affect the fiber's confinement loss, bend loss, and modality. For the fiber considered here, experimental results and simulations show that raising the gas pressure in the fiber core by 7 bars with respect to the cladding reduces confinement loss fivefold. There are several arenas where fully understanding and calibrating GDRI is essential. These include applications which require active control of the gas content within a HCF, including gas sensing and various non-linear optics applications. Furthermore, GDRI needs to be considered in HCF characterization, as immediately after fabrication the gas within the hollow core is at a pressure significantly below atmospheric [19]. For long fiber lengths, the core gas pressure will equalize to atmospheric over many days or weeks and the transmission of the HCF will change during this period, as the core will equalize faster than the cladding holes, creating a transient GDRI. In other applications, this technique has potential for increasing sensitivity and reducing the form factor of HCF-based sensors e.g., for trace gas detection [5,6] providing a means to control modality in power delivery [3], and optical gyroscopes [20,21], where high modal stability is desired. Finally, GDRI has potential to be applied as a new tool post-fabrication to create HCFs with combinations of optical properties that are so far not achievable using conventional approaches.

6. METHODS

A. Transmission Measurements

Light from a Fianium (NKT Photonics) supercontinuum source was coupled into the HCF via a butt-coupled LMA-15 launch fiber for mode field diameter matching. To establish a pressure gradient, the output end of the HCF was secured in a custom-designed gas cell filled with Argon gas at a gauge pressure of 6.7 bar (Fig. S2, Supplement 1). The gas cell has an integrated window that grants optical access from which the output beam can be collimated (via a free space lens arrangement) and then focused into a multi-mode fiber connected to a Yokogawa AQ-6315A optical spectrum analyzer (wavelength range 400–1750 nm). For all the measurements, the fiber was loosely wound on a 15 cm diameter spool under low tension.

Upon applying heat externally to a small section of the fiber, the thin silica membranes contract, causing the tubular capillary elements to collapse. Measurements in which solely the core region was pressurized were thus executed by collapsing the cladding tubes using an arc–fusion splicer as the point of the gas inlet. Figure S3(a) shows a side-on image of the fiber after the collapse where the microstructure tapers outwards from the collapse point which forms a waist. Cleaving at the taper waist results in the end-facet of the fiber being exposed with sealed capillary tubes, see Fig. S3(b), while leaving the core intact to allow the outcoupling of light, albeit with a reduced diameter of ∼14 μmSupplement 1. The collapsed end-facet is then contained in the gas cell. Note that in this work we did not focus on minimizing the loss of the cladding collapse technique, this being a proof of principle experiment. Other techniques, such as machining microchannels along the fiber between the cladding tubes via femtosecond laser processing [6], would allow the core to be selectively filled with gas while having a negligible negative impact on the fiber properties.

B. Numerical Simulations

The fiber modes were calculated using Comsol Multiphysics, a commercial finite element solver. The confinement loss of a given mode was obtained from the imaginary part of the effective index, and macro-bending losses calculated using the well-known conformal transformation to the index profile n_t via the refractive index profile n for a straight waveguide,

$$n_t = n e^{\frac{x}{R}} \sim n.\left(1+\frac{x}{R}\right), \tag{2}$$

where R is the bend radius of curvature [22]. Scattering and microbending contributions to the loss were neglected from the simulations. The simulated geometry was obtained from a SEM image of the tubular fiber cross section, see Fig. 1(a), using a MATLAB-based image analysis tool, by fitting circles to the inner and outer edges of individual capillary elements, thus determining their dimensions in addition to their azimuthal and radial positions. Slight adjustment of the membrane thickness (determined by conservation of mass from the fiber preform) was required to match the transmission window edges to experimental measurements, where the average membrane thickness for the simulated geometry was 446 nm, with a standard deviation of

7 nm, within the quoted experimental value (measured via SEM) of 440 ± 10 nm [23].

For the refractive index of the gas present in the core or capillaries for a given pressure n_{gas}, the Sellmeier expansion is

$$n_{gas}(\lambda, p, T) = \sqrt{1 + \frac{p}{p_0}.\frac{T_0}{T}.\left[\frac{B_1\lambda^2}{\lambda^2 - C_1} + \frac{B_2\lambda^2}{\lambda^2 - C_2}\right]_{p_0, T_0}}, \quad (3)$$

where p and p_0 are the gas pressure and atmospheric pressure, respectively, T is the temperature (fixed at 300 K), and $T_0 = 273.15\,K$. The Sellmeier coefficients for Argon were obtained from [24]. Assuming the core to be a circular bore and taking into account the gas compressibility, the pressure profile [and hence equivalent refractive index profile from Eq. (3)] established along the length of the fiber core (i.e., in the z-direction) that was created experimentally by applying ~7.7 bars of absolute pressure at the input end while keeping the output end open to atmospheric pressure can be written as [25]:

$$p(z) = \sqrt{p_2^2 - \frac{z}{L}(p_2^2 - p_1^2)}, \quad (4)$$

where p_2 is the inlet pressure (7.7 bar), p_1 is the outlet pressure (1 bar), and L (25 m) is the fiber length. In Fig. 4(c), the loss was integrated over this pressure profile for a range of inlet pressures p_2.

The average pressure along the fiber length $\bar{p}$ can be calculated as

$$\bar{p} = \frac{1}{L}\int_0^L p(z)\mathrm{d}z \approx 5.2 \text{ bar}. \quad (5)$$

The degree by which the thin silica membranes surrounding the core distort for the differential pressures considered in this paper was investigated by Comsol modeling. For a differential pressure of 5 bar (higher in the core), the distortion of the membranes was of the order 10^{-10} m, having a negligible effect on the fiber's optical properties.

Funding. Royal Society; Engineering and Physical Sciences Research Council.

Acknowledgment. The authors gratefully acknowledge support from EPSRC Programme grant "AirGuide Photonics". Furthermore, T.K. acknowledges support for his PhD studentship from IS-Instruments and N.V.W. gratefully acknowledges support from a Royal Society University Research Fellowship.

Disclosures. The authors declare no conflicts of interest.

Data availability. All data supporting this study are openly available from [26].

Supplemental document. See Supplement 1 for supporting content.

REFERENCES

1. G. T. Jasion, T. D. Bradley, K. Harrington, H. Sakr, Y. Chen, E. N. Fokoua, I. A. Davidson, A. Taranta, J. R. Hayes, D. J. Richardson, and F. Poletti, "Hollow core NANF with 0.28 dB/km attenuation in the C and L bands," in *Optical Fiber Communication Conference Postdeadline Papers* (2020), paper Th4B.4.
2. F. Poletti, N. V. Wheeler, M. N. Petrovich, N. Baddela, E. N. Fokoua, J. R. Hayes, D. R. Gray, Z. Li, R. Slavík, and D. J. Richardson, "Towards high-capacity fibre-optic communications at the speed of light in vacuum," Nat. Photonics **7**, 279–284 (2013).
3. M. Michieletto, J. K. Lyngsø, C. Jakobsen, J. Lægsgaard, O. Bang, and T. T. Alkeskjold, "Hollow core fibers for high power pulse delivery," Opt. Express **24**, 7103–7119 (2016).
4. M. Nikodem, G. Gomółka, M. Klimczak, D. Pysz, and R. Buczyński, "Demonstration of mid-infrared gas sensing using an anti-resonant hollow core fiber and a quantum cascade laser," Opt. Express **27**, 36350–36357 (2019).
5. S. Hanf, R. Keiner, D. Yan, J. Popp, and T. Frosch, "Fiber-enhanced Raman multi-gas spectroscopy: a versatile tool for environmental gas sensing and breath analysis," Anal. Chem. **86**, 5278–5285 (2014).
6. P. Zhao, Y. Zhao, H. Bao, H. L. Ho, W. Jin, S. Fan, S. Gao, Y. Wang, and P. Wang, "Mode-phase-difference photothermal spectroscopy for gas detection with an anti-resonant hollow-core optical fiber," Nat. Commun. **11**, 847 (2020).
7. P. St. J. Russell, P. Hölzer, W. Chang, A. Abdolvand, and J. C. Travers, "Hollow-core photonic crystal fibres for gas-based nonlinear optics," Nat. Photonics **8**, 278–286 (2014).
8. F. Yang, F. Gyger, and L. Thévenaz, "Intense Brillouin amplification in gas using hollow-core waveguides," Nat. Photonics **14**, 700–708 (2020).
9. J. C. Travers, T. F. Grigorova, C. Brahms, and F. Belli, "High-energy pulse self-compression and ultraviolet generation through soliton dynamics in hollow capillary fibres," Nat. Photonics **13**, 547–554 (2019).
10. J. C. Travers, W. Chang, J. Nold, N. Y. Joly, and P. St. J. Russell, "Ultrafast nonlinear optics in gas-filled hollow-core photonic crystal fibers [invited]," J. Opt. Soc. Am. B **28**, A11–A26 (2011).
11. F. Poletti, "Nested antiresonant nodeless hollow core fiber," Opt. Express **22**, 23807–23828 (2014).
12. W. Belardi and J. C. Knight, "Hollow antiresonant fibers with reduced attenuation," Opt. Lett. **39**, 1853–1856 (2014).
13. G. T. Jasion, D. J. Richardson, and F. Poletti, "Novel antiresonant hollow core fiber design with ultralow leakage loss using transverse power flow analysis," in *Optical Fiber Communication Conference (OFC)*, OSA Technical Digest (Optical Society of America, 2019).
14. G. T. Jasion, J. S. Shrimpton, Y. Chen, T. Bradley, D. J. Richardson, and F. Poletti, "Microstructure element method (MSEM): viscous flow model for the virtual draw of microstructured optical fibers," Opt. Express **23**, 312–329 (2015).
15. G. T. Jasion, J. R. Hayes, N. V. Wheeler, Y. Chen, T. D. Bradley, D. J. Richardson, and F. Poletti, "Fabrication of tubular anti-resonant hollow core fibers: modelling, draw dynamics and process optimization," Opt. Express **27**, 20567–20582 (2019).
16. E. A. J. Marcatili and R. A. Schmeltzer, "Hollow metallic and dielectric waveguides for long distance optical transmission and lasers," Bell Syst. Tech. J. **43**, 1783–1809 (1964).
17. R. Wynne and B. Barabadi, "Gas-filling dynamics of a hollow-core photonic bandgap fiber for nonvacuum conditions," Appl. Opt. **54**, 1751–1757 (2015).
18. H. Chen, R. van Uden, C. Okonkwo, Y. Jung, N. Wheeler, E. Fokoua, N. Baddela, M. Petrovich, F. Poletti, D. Richardson, O. Raz, H. de Waardt, and A. Koonen, 'Mode division multiplexing over 19-cell hollow-core photonic bandgap fibre by employing integrated mode multiplexer," Electron. Lett. **50**, 1227–1229 (2014).
19. S. Rikimi, Y. Chen, M. C. Partridge, I. A. Davidson, G. T. Jasion, T. D. Bradley, A. A. Taranta, F. Poletti, M. N. Petrovich, D. J. Richardson, and N. V. Wheeler, "Pressure in As-drawn hollow core fibers," in *OSA Advanced Photonics Congress (AP)* (2020), paper SoW1H.4.
20. M. J. F. Digonnet, H. K. Kim, S. Blin, V. Dangui, and G. S. Kino, "Sensitivity and stability of an air-core fibre-optic gyroscope," Meas. Sci. Technol. **18**, 3089–3097 (2007).
21. G. A. Sanders, A. A. Taranta, C. Narayanan, E. N. Fokoua, S. A. Mousavi, L. K. Strandjord, M. Smiciklas, T. D. Bradley, J. Hayes, G. T. Jasion, T. Qiu, W. Williams, F. Poletti, and D. N. Payne, "Hollow-core resonator fiber optic gyroscope using nodeless anti-resonant fiber," Opt. Lett **46**, 46–49 (2021).
22. M. Heiblum and J. H. Harris, "Analysis of curved optical-waveguides by conformal transformation," IEEE J. Quantum Electron. **11**, 75–83 (1975).
23. I. A. Davidson, M. Partridge, J. R. Hayes, Y. Chen, T. D. Bradley, H. Sakr, S. Rikimi, G. T. Jasion, E. N. Fokoua, M. Petrovich, F. Poletti, D. J. Richardson, and N. V. Wheeler, "Tubular anti-resonant hollow core fiber for visible Raman spectroscopy," Proc. SPIE **11206**, 1–312 (2019).
24. A. Börzsönyi, Z. Heiner, M. P. Kalashnikov, A. P. Kovács, and K. Osvay, "Dispersion measurement of inert gases and gas mixtures at 800 nm," Appl. Opt. **47**, 4856–4863 (2008).
25. C. Markos, J. C. Travers, A. Abdolvand, B. J. Eggleton, and O. Bang, "Hybrid photonic-crystal fiber," Rev. Mod. Phys. **89**, 045003 (2017).
26. T. W. Kelly, P. Horak, I. A. Davidson, M. Partridge, G. T. Jasion, S. Rikimi, A. Taranta, D. J. Richardson, F. Poletti, and N. V. Wheeler, "Dataset for article: 'Gas-induced differential refractive index enhanced guidance in hollow-core optical fibers'," University of Southampton Institutional Research Repository (2021), https://doi.org/10.5258/SOTON/D1736..